Lowland Technology International 2018; 20 (3): 259-272
International Association of Lowland Technology (IALT): ISSN 1344-9656

Research Paper

A nonlinear analysis for GRS walls conceiving kinematics of failure against pullout

S. Patra [1] and J. T. Shahu [2]

ARTICLE INFORMATION

Article history:

Received: 03 January, 2017
Received in revised form: 21 March, 2017
Accepted: 03 April, 2017
Publish on: 07 December, 2018

Keywords:

GRS structures
Nonlinear analysis
Pasternak model
Kinematics of failure
Finite difference method

ABSTRACT

A modified nonlinear analysis is presented to investigate the pullout response of geosynthetic reinforced soil (GRS) walls. The analysis conceives a hyperbolic stress-strain relationship for the backfill, the kinematics of the failure and the deformation compatibility between the soil and the reinforcement. The deformation compatibility is incorporated by introducing an updated discretization technique, and the true projected length of the reinforcement after deformation is evaluated by a simple computational scheme. A case study is presented for an instrumented full-scale reinforced soil wall to validate the present analysis. The maximum tension in the reinforcement at each level is computed considering the effect of compaction, and the results are compared with the measured values and those predicted by AASHTO simplified method. The comparison shows that the present analysis gives a better estimation of the reinforcement tension thus can be easily integrated with the existing method. A parametric study is also conducted mainly to determine the effect of stiffness and strength parameters of the subgrade which have a significant influence on the design of GRS walls against pullout failure for all practical applications.

1. Introduction

During the last few decades or so, geosynthetics reinforced soil (GRS) structures, such as reinforced soil walls (**Fig. 1a**) and embankments (**Figs. 1b-c**), have emerged as sustainable alternatives to the conventional concrete or masonry retaining structures (Damians et al., 2016; Kargar and Hosseini, 2016; Sowmiya et al., 2015; Won et al., 2016). One of the major advantages of these structures is inherent flexibility that allows a considerable deformation before failure (Ahmad and Choudhury, 2012; Desai and El-Hoseiny, 2005; Liu, 2016; Ouria et al., 2016; Won et al., 2016). At large deformation, the subgrade soil and soil-reinforcement interface both exhibit a distinctly nonlinear behaviour. However, conventional design methods are empirical in nature and do not consider the nonlinear behaviour of the subgrade and proper soil-reinforcement interface response resulting a high level of conservatism in the design (Allen and Bathurst, 2013; Liu, 2016; Ouria et al., 2016; Rowe and Ho, 1993; Yu et al., 2016). Besides, these methods do not consider localized mobilization (Bobet et al., 2007; Gao et el., 2014; Gurung et al., 1999; Madhav and Umashankar, 2003a-b; MacLaughlin et al., 2001; Patra and Shahu, 2015a-b) of reinforcement tension and its direction in the vicinity of the failure surface.

The localized tension mobilized in the reinforcement depends on the kinematics of failure (Gao et al., 2014;

[1] Assistant Professor, School of Infrastructure, Indian Institute of Technology Bhubaneswar, Argul, Jatni 752050, INDIA, shantanupatra@iitbbs.ac.in
[2] Professor & IALT member, Department of Civil Engineering, IIT Delhi, New Delhi 110016, INDIA, shahu@civil.iitd.ac.in
Note: Discussion on this paper is open until June 2019

MacLaughlin et al. 2001; Madhav and Umashankar, 2003a-b; Patra and Shahu, 2012-2015a-b; Sitar et al., 2005) that suggests the failure surface intersecting the reinforcement obliquely. Thus, the reinforcement is subjected to an oblique pullout force *P* as shown in **Fig. 1(d)**. Under the action of the oblique pull *P*, the reinforcement undergoes transverse deformation and mobilizes additional normal and shear stresses at soil-reinforcement interface. Consequently, the pullout capacity of the reinforcement increases and becomes greater than the axial pull.

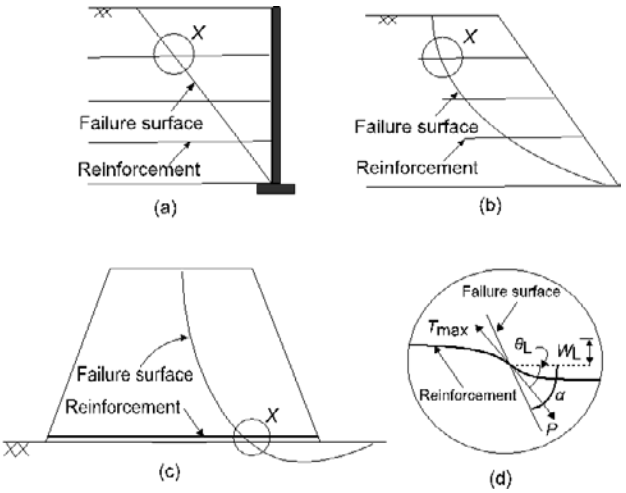

Fig. 1. Kinematics of failure of reinforced structures: (a) reinforced soil wall; (b) reinforced slope; (c) embankment; and (d) enlarged view at X.

2. Background

The pullout response under a known value of transverse end displacement was first studied by Madhav and Umashankar (2003a-b). Since the analysis does not consider the overall equilibrium of forces, it is valid only for small end displacement (Shahu, 2007-2008). Moreover, the proposed model suffers from the inherent drawbacks associated with the Winkler spring based model that do not consider the interaction between neighbouring springs. Consequently, the analysis overestimates the magnitude and direction of the mobilized localized reinforcement tension (Allen and Bathurst, 2013; Gao et al., 2014; Patra and Shahu, 2015a-b; Patra and Shahu 2014; Sitar et al., 2005) as equal to that of the pullout force, which is not true as suggested by the experimental findings (Bergado et al., 2000; Shewbridge and Sitar,1989).

Patra and Shahu (2012) introduced the effect of the subgrade shear stiffness in the pullout analysis by assuming a linear elastic Pasternak subgrade. Pasternak model (Deb et al., 2007; Madhav and Poorooshasb, 1988-89; Poorooshasb et al., 1985; Shukla and Chandra 1994; Tanahashi 2007) based analysis somewhat succeeded in removing the existing discrepancies between the experimental results and the Winkler based model in predicting the localized reinforced soil behaviour.

The major limitation of the earlier model (Patra and Shahu, 2012-2015a-b; Gao et al., 2014; Shahu, 2007-2008) is the assumption of a constant value of the projected length equal to the initial length *L* of the reinforcement along the horizontal direction for discretization. However, as the reinforcement undergoes transverse deformation, the horizontal component of the projected length changes (**Figs. 2a-c**) and therefore should be accounted for in the analysis. The lack of corroboration against full-scale reinforced soil walls is another major shortcomings. While Patra and Shahu (2015a,b) validated their analysis using published small-scale laboratory model tests data (Lee et al., 1973; Juran and Christopher, 1989), till date no effort has been made to validate the results with a full-scale reinforced soil wall (Allen and Bathurst, 2013; Bathurst et al., 2009) conceiving obliquity of the pullout force.

In practice, the reinforcement may undergo a significant deformation particularly in the vicinity of the failure surface before the pullout. Thus, the assumption of a linear subgrade (Patra and Shahu, 2012-2015a; Shahu, 2007) may not be proper as it may yield a potentially conservative value of end displacement, reinforcement tension, and the factor of safety against pullout (Patra and Shahu, 2012).

In this paper, a modified nonlinear analysis is presented to investigate the pullout response of geosynthetic reinforced soil (GRS) walls. The analysis conceives a nonlinear hyperbolic stress-strain relationship for the backfill, kinematics of the failure and the deformation compatibility between the soil and the reinforcement. The deformation compatibility is incorporated by introducing an updated discretization technique. The true projected length of the reinforcement after deformation, which is essential for the accurate estimation of the pullout capacity, is evaluated by a simple computational scheme. A case study is presented for an instrumented full-scale reinforced soil wall to validate the present analysis. The maximum tension in the reinforcement at each level is computed considering the effect of compaction, and the results are compared with the measured values and those predicted by AASHTO simplified method. A parametric study is also conducted mainly to determine the effect of the controlling nonlinear response factors (in shear ξ and in compression β) on the pullout capacity.

3. Problem definition and analysis

An inextensible sheet reinforcement of length L is resting on a nonlinear elasto-plastic subgrade at depth D (**Fig. 2a**). The reinforcement is subjected to an oblique pull P at point B where the sliding mass intersects the reinforcement at an angle α to the horizontal (**Figs. 1a-d**). Under the action of the oblique pull P, the mobilized maximum tension in the reinforcement is T_{max} acting in the direction θ_L with the horizontal at end B, where the vertical displacement is w_L. **Figure 2(b)** shows the proposed model for the analysis and **Fig. 2(c)** shows the forces acting on the deformed reinforcement.

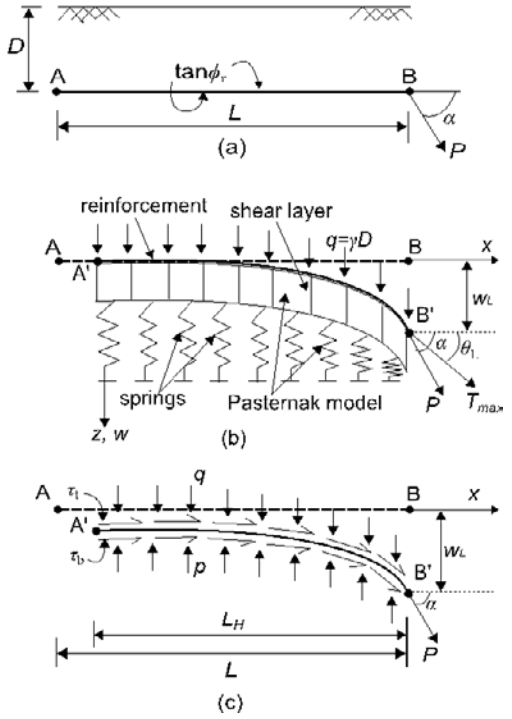

Fig. 2. Schematic of the model used: (a) reinforcement subject to oblique pull; (b) deformed model; and (c) forces on the reinforcement.

The reinforcement is assumed as inextensible rough membrane. For some reinforcements (like geogrids), and for low overburden pressures, this assumption is justified. It may be noted that the extensibility of the reinforcement in GRS walls is mainly governed by the reinforcement stiffness factor $J^* = J/(2\gamma D L_e \tan\phi_r)$ (Shahu and Hayashi 2009), which in turn depends on reinforcement stiffness J, overburden pressure γD, the effective length of reinforcement L_e and soil-reinforcement interface friction angle ϕ_r. For J^*>15, the reinforcement exhibits inextensible behavior (Shahu and Hayashi 2009). In the present analysis, J^* varies from 18 to 56 for the top reinforcement where the pullout occurs and thus the reinforcement behaves as an inextensible membrane (Liu 2016). The underlying soil and the overlying soil (of unit weight γ) are represented by a nonlinear Pasternak model and overburden stress, respectively.

Nonlinear Pasternak model incorporates the hyperbolic stress-strain relationships into the basic Pasternak model where the Pasternak model introduces a shear interaction between the compressible soil elements (springs) by providing a top shear layer (**Fig. 2b**). The resulting governing equation is given by (Ghosh and Madhav, 1994).

$$p - q = \frac{k_s w}{1+\frac{k_s w}{q_{ult}}} - \frac{GH}{\left(1+\frac{G}{\tau_{ult}}\frac{\partial w}{\partial x}\right)^2}\frac{\partial^2 w}{\partial x^2} \qquad [1]$$

where q and p are stresses at the top and bottom of the reinforcement (**Figs. 3a and b**); k_s and q_{ult} are the initial slopes of the vertical stress-displacement curve and the ultimate normal stress of the subgrade (**Fig. 3c**); G and τ_{ult} are the initial slopes of the shear stress-shear strain curve and the ultimate shear stress of the subgrade (**Fig. 3d**); H is the thickness of the shear layer (**Fig. 3b**); and w is the vertical displacement at any point x along the reinforcement. q is the normal stress on the top of the reinforcement resulting from the overburden pressure whereas p is the normal stresses acting at the bottom of the reinforcement caused by the combined effect of overburden q and the stress generated due to the downward component of the pullout force. Consequently, the total stress p acting at the bottom of the reinforcement may be significantly greater than the overburden pressure q at the reinforcement level.

A rigid-plastic behaviour is assumed for soil-reinforcement interface (Patra and Shahu, 2012). The mobilized shear stresses τ along the soil-reinforcement interface are evaluated as:

$$\tau = \tau_t + \tau_b \qquad [2]$$

where $\tau_t = q\cos\theta_c \tan\phi_r$; $\tau_b = p\cos\theta_c \tan\phi_r$; q and p are normal stresses acting at the top and bottom of the reinforcement, respectively; θ_c is an average inclination of the reinforcement element with the horizontal and ϕ_r is soil-reinforcement interface friction angle.

In the proposed model, the final deformed shape of the reinforcement is considered for the equilibrium of forces as shown in **Fig. 2(c)**. An updated discretization technique is adopted in the analysis to account for the exact deformed shape of the reinforcement. As the reinforcement undergoes a transverse displacement, the projected length L_H along the horizontal direction also changes (**Fig. 2c**). Thus, in the present analysis, the discretization is done at each step over the modified length of the reinforcement.

In the present formulation, the geosynthetics is assumed as an inextensible reinforcement hence the

total length of the reinforcement is constant. The reinforcement changes its shape from initial straight horizontal position to a curved shape due to the transverse (downward) deformation while keeping the total length unchanged. Therefore, the projected horizontal length of the reinforcement reduces though the total length L of the reinforcement still remains the constant. For example, an inextensible reinforcement of length L if simply rotated from its horizontal position to an angle, say θ, the horizontal component of the length L_H will change from the initial L_H=L to L_{H1}, where L_{H1} (= L_H cos θ) is always less than the original straight length L.

3.1 Equilibrium of forces on soil-reinforcement element

Figure 3(a) shows a reinforcement element of deformed horizontal length Δx and unit width. The reinforcement tensions and inclinations at horizontal distances x and (x+Δx) are T and θ, and (T+ΔT) and ($\theta+\Delta\theta$), respectively.

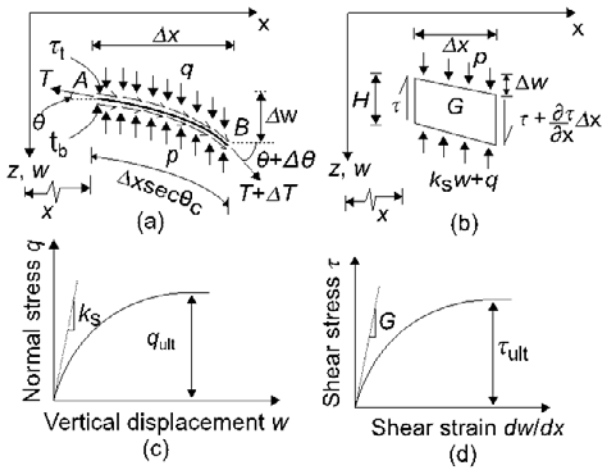

Fig. 3. Stresses on soil-reinforcement element and constitutive relationship: (a) stresses on reinforcement element; (b) stresses on Pasternak shear layer element; (c) normal stress-displacement relationship for Winkler springs; and (d) shear stress-strain relationship for Pasternak shear layer.

Applying the vertical and the horizontal force equilibrium to the final deformed shape of the reinforcement element (**Fig. 3a**) next, substituting (p-q), and ($\tau_t+\tau_b$) from Eq. (1) and (2), respectively into the governing differential equation (Patra and Shahu, 2012) and simplifying, one gets

$$T\cos^2\theta\frac{\mathrm{d}^2w}{\mathrm{d}x^2}=\frac{k_sw}{1+\dfrac{k_sw}{q_{ult}}}-\frac{GH}{\left(1+\dfrac{G}{\tau_{ult}}\dfrac{\partial w}{\partial x}\right)^2}\frac{\partial^2w}{\partial x^2} \qquad [3]$$

$$\frac{\mathrm{d}T}{\mathrm{d}x}=\left\{\frac{k_sw}{1+\dfrac{k_sw}{q_{ult}}}-\frac{GH}{\left(1+\dfrac{G}{\tau_{ult}}\dfrac{\partial w}{\partial x}\right)^2}\frac{\partial^2w}{\partial x^2}\right\}\tan\theta + \left\{\frac{k_sw}{\left(1+\dfrac{k_sw}{q_{ult}}\right)}-\frac{GH}{\left(1+\dfrac{G}{\tau_{ult}}\dfrac{\partial w}{\partial x}\right)^2}\frac{\partial^2w}{\partial x^2}+2\gamma d\right\}\tan\phi_r \qquad [4]$$

Assuming a long reinforcement, the boundary conditions are found to be (**Fig. 2b**): at x = 0 (end A), dw/dx= 0 and T = 0; and at x = L (end B), w = w_L. Few trial analyses were also carried out considering the left-hand side boundary beyond 5-10 times the length of the reinforcement that confirms the current assumption dw/dx= 0 at A is correct.

A finite difference method is then adopted to solve the Eqs. (3) and (4). These equations are first normalized as: X = x/L, W = w/w_L, W_L = w_L/L, P^* = P/T_{HP}, T^* = T/T_{HP}, p^* = p/γD, q^* = q/γD, $\tau_t^*=\tau_t/\gamma D$ and $\tau_b^*=\tau_b/\gamma D$; where $T_{HP}=2\gamma DL\tan\phi_r$ is the axial pullout capacity of the reinforcement. Next, the forward and central difference schemes are used for discretizing the first and second order derivative terms, respectively. Finally, simplifying, one gets

$$W_i=\frac{n^2\left(\left\{\dfrac{2\tan\phi_rT_i^*\cos^2\theta_i}{+\left\{\dfrac{G^*}{\left(\left[1+\xi W_L\dfrac{\partial W_i}{\partial X}\right]\right)^2}\right\}}\right)(W_{i+1}+W_{i-1})}{\dfrac{\mu}{1+\beta W_LW_i}+2n^2\left(\left\{\dfrac{2\tan\phi_rT_i^*\cos^2\theta_i}{+\left\{\dfrac{G^*}{\left(\left[1+\xi W_L\dfrac{\partial W_i}{\partial X}\right]\right)^2}\right\}}\right)} \qquad [5]$$

$$T_{i+1}^*=\left\{\frac{\mu W_LW_i}{1+\beta W_LW_i}-\frac{W_LG^*}{\left(1+\xi W_L\dfrac{\partial W_i}{\partial X}\right)^2}\frac{\partial^2W_i}{\partial X^2}\right\}\times \left\{\frac{\tan\theta_i}{\tan\phi_r}+1\right\}\frac{1}{2n}+\frac{1}{n}+T_i^* \qquad [6]$$

where $\theta_i=(\theta_{ci}+\theta_{ci-1})/2$; $\theta_{ci}=\tan^{-1}\left[nW_L(W_{i+1}-W_i)\right]$; $\mu=k_sL/\gamma D=$ subgrade normal stiffness factor; $\beta=k_sL/q_{ult}=$ nonlinear subgrade response factor in

vertical compression; $G^*=GH/\gamma DL=$ subgrade shear stiffness factor; $\xi=G/\tau_{ult}=$ nonlinear subgrade response factor in shear; $W_L=w_L/L=$ normalized end displacement; W_i and T_i^* are normalized displacement and reinforcement tension, respectively, at node *i*; and *n* is the number of elements into which the reinforcement strip is divided (i.e., $\Delta X=1/n$). The boundary conditions become

At $X = 0$, $dW/dX = 0$ and $T^* = 0$; and at $X = 1$, $W = 1$ (7)

3.2 Overall equilibrium of forces

Applying overall equilibrium of external forces in the vertical and horizontal directions to the final deformed shape of the reinforcement (**Figs. 2c and 3a**), next normalizing and discretizing the resulting equations into the finite difference form and simplifying (Patra and Shahu, 2012-2015a,b), one gets

$$P^*\sin\alpha=\frac{1}{2n\tan\phi_r}\sum_{i=1}^{n}\left\{\left(\begin{array}{l}\left(\frac{\mu W_L W_i}{1+\beta W_L W_i}\right)\sec\theta_{ci}+\\ \frac{\mu W_L W_i}{1+\beta W_L W_i}-\\ \frac{G^*W_L}{\left(1+\xi W_L\frac{\partial W_i}{\partial X}\right)^2}\frac{\partial^2 W_i}{\partial X^2}+2\end{array}\right)\sin\theta_{ci}\tan\phi_r\right\} \quad [8]$$

$$P^*\cos\alpha=\frac{1}{2n\tan\phi_r}\sum_{i=1}^{n}\left\{\left(\begin{array}{l}\frac{\mu W_L W_i}{1+\beta W_L W_i}-\\ \frac{G^*W_L}{\left(1+\xi W_L\frac{\partial W_i}{\partial X}\right)^2}\frac{\partial^2 W_i}{\partial X^2}+2\end{array}\right)\cos\theta_{ci}\tan\phi_r\right\} \quad [9]$$

where $P^* = P/2\gamma DL\tan\phi_r$ = normalized oblique pullout capacity. Finally, the obliquity α and the pullout force P^* can be obtained from the following expressions

$$\tan\alpha=\frac{\sum_{i=1}^{n}\left\{\left(\begin{array}{l}\left(\frac{\mu W_L W_i}{1+\beta W_L W_i}\right)\sec\theta_{ci}+\\ \frac{\mu W_L W_i}{1+\beta W_L W_i}-\\ \frac{G^*W_L}{\left(1+\xi W_L\frac{\partial W_i}{\partial X}\right)^2}\frac{\partial^2 W_i}{\partial X^2}+2\end{array}\right)\sin\theta_{ci}\tan\phi_r\right\}}{\sum_{i=1}^{n}\left\{\left(\begin{array}{l}\frac{\mu W_L W_i}{1+\beta W_L W_i}-\\ \frac{G^*W_L}{\left(1+\xi W_L\frac{\partial W_i}{\partial X}\right)^2}\frac{\partial^2 W_i}{\partial X^2}+2\end{array}\right)\cos\theta_{ci}\tan\phi_r\right\}} \quad [10]$$

$$P^*=\frac{1}{2n\cos\alpha}\sum_{i=1}^{n}\left\{\left(\begin{array}{l}\frac{\mu W_L W_i}{1+\beta W_L W_i}-\\ \frac{G^*W_L}{\left(1+\xi W_L\frac{\partial W_i}{\partial X}\right)^2}\frac{\partial^2 W_i}{\partial X^2}+2\end{array}\right)\cos\theta_{ci}\right\} \quad [11]$$

where $\theta_i=\left(\theta_{ci}+\theta_{ci-1}\right)/2$. The horizontal pullout capacity P_H^* is then evaluated as $P_H^*=P^*\cos\alpha=T_{\max}^*\cos\theta_L$; where $T_{\max}^*$ and θ_L = maximum reinforcement tension and its direction at node *n*+1, i.e. $T_{\max}^*=T_{n+1}^*$ and $\theta_L=\theta_{n+1}$).

3.3 Solution

Solution to the above formulation is obtained by determining four sets of unknown variables, namely, W_i, T_i^*, W_L and P^* from four sets of known equations; i.e. two sets of elemental equilibrium equations and, two overall equilibrium equations. The elemental equilibrium equations (Eqs. 5 and 6) are solved in conjunction with, the boundary conditions (Eq. 7) and the overall equilibrium equations (Eqs. 8 and 9), to obtain the normalized displacement W_i and tension T_i^* at all nodes, the end displacement W_L, and the pullout capacity P^*. The solution involves a trial and error approach and requires input parameters e.g. subgrade shear stiffness factor G^*, subgrade normal stiffness factor μ, nonlinear subgrade response factor in shear ξ, nonlinear subgrade response factor in vertical compression β, interface frictional resistance ϕ_r and obliquity α of the pullout force.

3.4 Deformation compatibility and updated discretization

The present analysis considers an inextensible reinforcement of length *L*. For inextensible reinforcement, the deformed length *S* ($=\int ds$, where *ds* is the elemental length of the deformed reinforcement) should always remain constant (i.e., equal to the initial length of the reinforcement *L*). If the reinforcement is subjected to any transverse displacement *w*, it should deform in such a manner that the projected horizontal length L_H of the reinforcement and the discretized length ($=L_H/n$, where *n* is the number of reinforcement element) reduces in order to keep the total deformed length a constant (=*L*).

The projected horizontal length may be estimated as $L_H=\int ds\cos\theta$, which is a function of reinforcement slope θ. In general, higher the values of the transverse deformation *w*, higher will be the reinforcement slope θ, and lesser will be the L_H and the discretized length. However, existing methods (Patra and Shahu, 2012-2015a, 2015b; Gao et al., 2014; Shahu, 2007-2008) neglect the deformation compatibility and assumes a constant value of the projected length L_H (=*L*) and the discretized length which should change with the change in the transverse deformation. Consequently, these methods result in a higher value of the total deformed reinforcement length $S=\int L_H Sec\theta$ as compared to the true length. As the pullout capacity is a function of mobilized interface resistance over the deformed length *S*,

the incorrect estimation of the deformed length S leads to a gross error in assessing the pullout capacity.

In the present analysis, the discretization is redone with respect to the corrected value of the projected length $L_{H,\,new}$ and it has been obtained iteratively by applying the compatibility criteria as

$$L_{H,new} = L_H \, L \Big/ \sum \frac{L_H}{n} \sec\theta_{ci} \qquad [12]$$

For each successive iteration, the discretization is repeated with respect to the new value of the projected length $L_{H,\,new}$, i.e., discretized length = $L_{H,\,new}/n$. The above process is continued until the convergence is achieved ($L_{H,new} \approx L_H$).

4. Case study of a full scale reinforced soil wall

In this section, the results of an instrumented full-scale reinforced soil wall (Bathurst et al., 2009) are compared to demonstrate the application of the present analysis in the design of reinforced soil walls. Bathurst et al. (2009) reported four instrumented walls (**Fig. 4**) built and designed to satisfy National Concrete Masonry Association guidelines (NCMA 1996) at Royal Military College (RMC). Since the present analysis is valid for inextensible reinforcement, Wall No. 6 which was reinforced with welded wire mesh (WWM) is considered for the comparisons. The wall was constructed with six layers of reinforcement with a vertical spacing S_V= 0.6 m and a target facing batter ω = 8° from the vertical (**Fig. 4**). Uniformly graded, naturally deposited rounded beach sand was used as backfill. The measured bulk unit weight γ of the backfill material is 17.2 kN/m^3 (compacted using heavy compaction), and the peak plane-strain friction angle ϕ is reported as 44° (Bathurst et al. 2005).

The maximum reinforcement tensions T_{max} at each reinforcement level are evaluated, and the results are compared with the measured values (Bathurst et al., 2009), AASHTO (2002) Simplified Method and Patra and Shahu (2012).

According to AASHTO (2002) Simplified Method (Bathurst et al., 2009), the maximum reinforcement load T_{max} is obtained as

$$T_{max} = K\gamma z S_V \qquad [13]$$

where z is the depth of the reinforcement layer below the crest of the wall, the active earth pressure coefficient $K = \cos^2(\phi+\omega) \Big/ \cos^2\omega\left[1+\sin\phi/\cos\omega\right]^2$, ω = target facing batter from the vertical, and ϕ = the peak plane-strain friction angle of the soil.

The maximum reinforcement load T_{max} can be calculated using the proposed analysis as

$$T_{max} = T^*_{max} K\gamma z S_V \qquad [14]$$

where values of T^*_{max} may be obtained from the solution of equations 5-11 and are shown in Table 1, and all others parameters remain same as defined previously.

Figure 5 shows the variation of maximum reinforcement load with the depth of the reinforcement at the end of construction for RMC Wall No. 6. The measured data (**Fig. 5**) indicates that the tension in the top two layers of reinforcement increases and then decreases subsequently. AASHTO (2002) Simplified Method, and Patra and Shahu (2012) underpredict the reinforcement load as low as 50 % of the measured maximum tension for top few reinforcements. However, for inextensible reinforcement, the top few reinforcements are most critical against the pullout. Thus, the present analysis gives a better prediction of the reinforcement load as compared to the AASHTO (2002), and Patra and Shahu (2012).

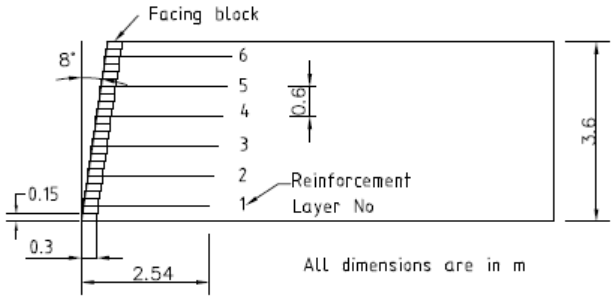

Fig. 4. Schematic diagram of instrumented full-scale reinforced soil walls (Bathurst et al. 2009).

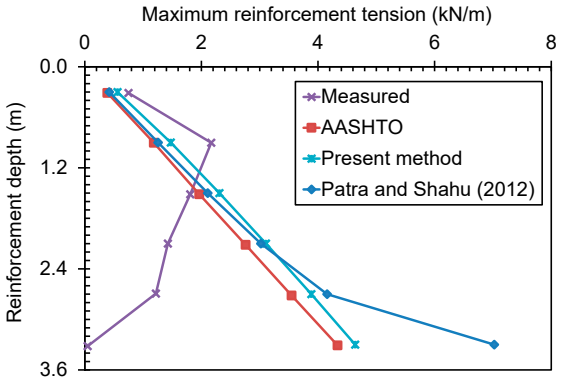

Fig. 5. Measured maximum reinforcement tension at each reinforcement level.

For prediction of reinforcement loads in the wall (Wall No. 6), the Reinforcement is assumed as inextensible rough membrane and all other required parameters are shown in Table 1. In the case of Patra and Shahu (2012), the model parameters β and ξ are assumed as equal to zero. The effect of heavy compaction is also considered by incorporating an equivalent surcharge of 8 kPa in addition to the overburden pressure due to the backfill

(Huang et al., 2009). A linear failure surface is assumed that passes through the toe of the wall making an angle α = 45+ϕ/2° with the horizontal (refer FHWA-NHI-00-043, Elias et al., 2001). However, the analysis is not only applicable to Rankine's surface (which has been assumed here for simplification) but for any failure surfaces (e.g. two-part wedge, circular or log spiral).

Table 1. Parameters used for back-prediction of reinforcement loads

Layer *i*	z	H_0	G*	μ	β	ξ	T^*_{max}
1	0.3	3.3	1866.8	9469.5	97.7	3221.9	1.36
2	0.9	2.7	475.3	4132.3	127.9	1002.7	1.19
3	1.5	2.1	195.8	3611.1	186.3	531.1	1.12
4	2.1	1.5	89.4	4034.3	291.4	339.5	1.07
5	2.7	0.9	37.8	5778.4	536.7	239.0	1.04
6	3.3	0.3	9.4	15530.1	1763.0	178.6	1.02

Note: H_0= Subgrade thickness, Depth=z, (Bathurst, et al., 2009).

4.1 Limitations

Bathurst et al. (2009) measured maximum reinforcement tension with depth at the end of construction for an instrumented full scale reinforced soil wall (Wall No. 6). There is no failure hence Bathurst et al. (2009) call this as 'working stress condition'. The present analysis is carried out assuming limit state condition (soil is on the verge of failure). Based on the results of the analysis, the reinforcement tension is calculated. This is not strictly compatible with the working stress method and is one of the limitations of the present approach. However, it may be noted that the FHWA method (FHWA 2001) calculates the reinforcement tension using active earth pressure assumption which also represents the limit state condition (active earth pressure is obtained on the verge of soil failure). The researchers have traditionally compared this limit state tension in the reinforcement with the measured working stress tension. In fact, in this paper, the same FHWA equation has been modified by a reinforcement tension factor T^*_{max} (Eq. 14) and used for comparison.

5. Parametric study and range of parameters

The results are found to converge for $n \geq 1000$, where n is the number of discretized elements. Hence, n = 1000 has been adopted for the present analysis. A parametric study is conducted considering the following model parameters: subgrade shear stiffness factor $G^*(=GH/\gamma DL)$, subgrade normal stiffness factor $\mu(=k_sL/\gamma D)$, nonlinear subgrade response factor in shear $\xi(=G/\tau_{ult})$, nonlinear subgrade response factor in vertical compression $\beta(=k_sL/q_{ult})$, angle of interface frictional resistance ϕ_r and obliquity α. The effect of the above parameters on the pullout responses are quantified in terms of horizontal pullout capacity P^*_H, maximum reinforcement tension T^*_{max}, end displacement W_L and end inclination θ_L. The results are also compared with the linear-elastic model proposed by Patra and Shahu (2012).

The ranges of parameters used in the analysis are: D = 1-10 m, L = 1-10 m, modulus of elasticity E_s = 10-81 kPa (corresponding to sand in the loose to dense state), Poisson's ratio v = 0.3, γ = 15-20 kN/m^3; ϕ_r = 20-45°; q_{ult} = 100-400 kPa, τ_{ult} = 8.66-200 kPa and α = 0-90°. The shear layer thickness H (= 0.09-0.54 m), the subgrade shear modulus G (= 3,846-31,154 kPa), and the spring constant k_s (= 2,692-109,038 kN/m^3) are determined following Patra and Shahu (2012). Based on the above parameters and the practical considerations (Patra and Shahu, 2012; Shahu, 2007-2008), μ = 500-5000, G^* = 0-1000, β=0-3000 and ξ = 0-2000 are adopted for the parametric study. The effect of any particular parameter on the soil-reinforcement responses is then studied by varying the same against the nominal set: G^* = 10, μ =1000, ξ=100, β = 100, ϕ_r = 30° and α = 60°.

6. Localızed reınforced soıl-response

6.1 Effect of nonlinear subgrade response factor in shear ξ

For a given value of shear modulus G, a higher value of nonlinear subgrade response factor in shear $\xi(=G/\tau_{ult})$ indicates a lower value of the ultimate failure shear stress τ_{ult} and a highly non-linear response of the subgrade in shear. **Figs. 6-7** shows the variations of the horizontal component of the pullout force P^*_H, mobilized maximum reinforcement tension T^*_{max}, end displacement W_L and end angle θ_L in response to the changes in nonlinear subgrade response factor in shear ξ. As ξ increases, all the responses, P^*_H, T^*_{max}, W_L and θ_L increase. However, after a particular value of ξ, the above responses reach a constant value (**Figs. 6-7**) since, for higher ξ, full mobilization of shear stresses takes place between the neighbouring soil elements. The value of ξ at which all these responses becomes constant, increases for higher values of G^* (**Figs. 6-7**).

For higher ξ, Pasternak shear layer ceases to distribute the vertical component of the pullout force over a larger area because of shear failure between the neighbouring soil elements, causing a localized distribution of the normal stresses at the soil-reinforcement interface; consequently, the interface shear stresses increases. Higher the interface shear stresses, higher is the horizontal component of the

pullout force P_H^* (**Fig. 6a**). A higher value of P_H^* indicates a higher value of the maximum reinforcement tension $T_{\max}^*$ (**Fig. 6b**) and the pullout capacity P^*. A higher pullout force ultimately results in a higher end-displacement W_L (**Fig. 7a**) and end angle θ_L (Fig. 7b).

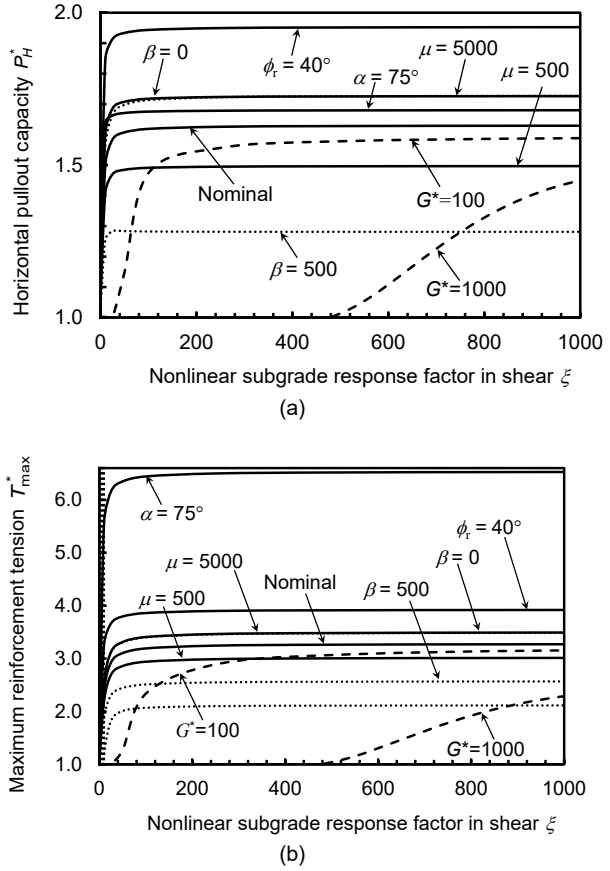

Fig. 6. Variation of (a) horizontal pullout capacity factor P_H^* ; and (b) maximum reinforcement tension $T_{\max}^*$ with the nonlinear subgrade response factor in shear ξ (Nominal case: G^*=10, μ=1000, β=100, ϕ_r=30°, α=60°).

Figure 7(b) shows that the direction θ_L of the reinforcement tension at the pullout end sharply increases and becomes almost equal to the obliquity of the pullout force (i.e. end angle $\theta_L \approx \alpha$) for the subgrade having a lower shear stiffness (lower $G^*$and higher ξ). On the other hand, a stiffer subgrade (higher G^* and lower ξ) produces a lower value of the end angle θ_L as compared to the obliquity of the pullout force α (**Fig. 7b**), because, displacements, in this case, become more uniform along the length of the reinforcement. The above finding is also validated experimentally by Bergado et al. (2000) and Shewbridge and Sitar (1989). However, the normal stiffness μ and strength q_{ult} of the subgrade have a negligible effect on the end angle (**Fig. 7b**).

Figures 6-7 also show that as the angle of interface friction ϕ_r increases, all the responses namely, the horizontal component of the pullout force P_H^* , end displacement W_L and end angle θ_L increases. As the angle of interface friction ϕ_r increases, the soil-reinforcement interface mobilizes additional shear stresses causing a higher reinforcement tension and the pullout force (**Figs. 6a-b**). A higher pullout force gives rise to a higher end displacement W_L (**Fig. 7a**) and end angle θ_L (**Fig. 7b**).

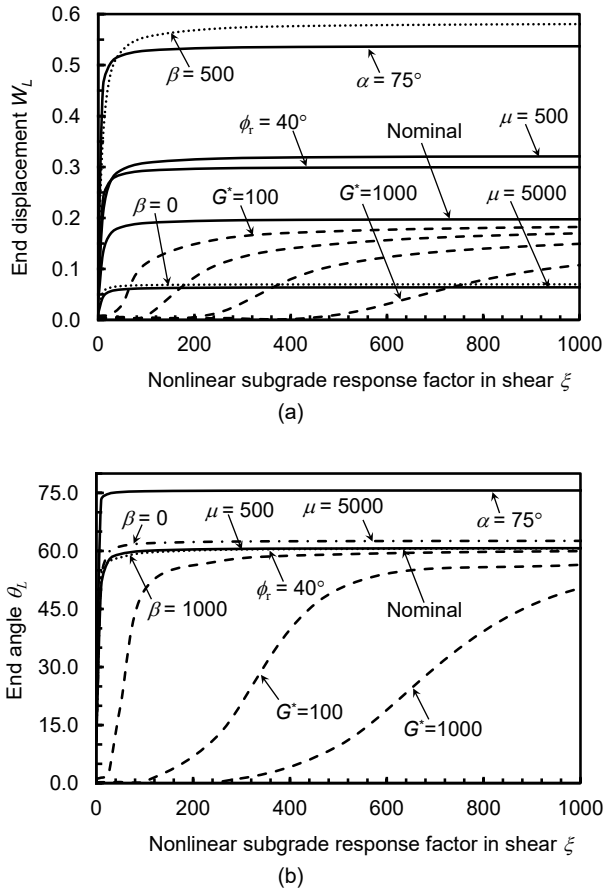

Fig. 7. Variation of (a) end-displacement W_L; and (b) end-angle θ_L with the nonlinear subgrade response factor in shear ξ (Nominal case: G^*=10, μ=1000, β=100, ϕ_r=30°, α=60°).

6.2 Effect of nonlinear subgrade response factor in vertical compression β

Higher the value of the nonlinear subgrade response factor in vertical compression β (= k_sL/q_{ult}),higher is the non-linearity in the subgrade response in vertical compression and weaker is the subgrade, i.e., lower is the ultimate bearing resistance q_{ult} for a given value of Winkler's spring constant k_s. **Figure 8(a)** shows that, as nonlinear subgrade response factor in vertical compression β increases, the horizontal component of the pullout capacity P_H^* decreases and, the rate of decrease is higher at lower values of β. But, after a certain value of β, P_H^* becomes almost constant since

the bearing resistance against vertical compression q_{ult} is fully mobilized.

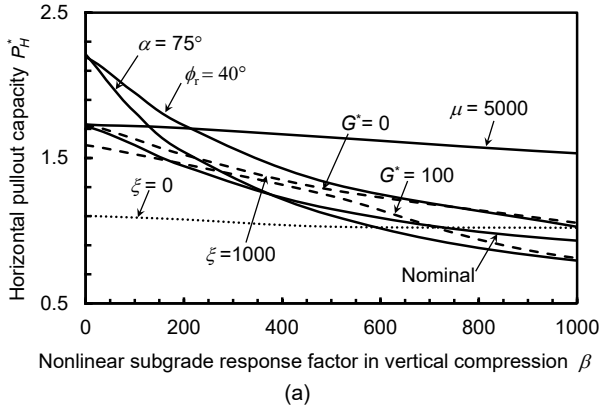

Fig. 8. Variation of (a) horizontal pullout capacity factor P_H^* ; and (b) end-displacement W_L with the nonlinear subgrade response factor in vertical compression β (Nominal case: G^*=10, μ=1000, ξ=100, ϕ_r=30°, α=60°).

As, for higher values of β (or weaker subgrade), the displacements become more uniform and normal stresses are distributed over a greater length of the reinforcement, the horizontal component of pullout capacity P_H^* decrease (**Fig. 8a**). On the other hand, stronger subgrade (lower values of β) gives rise to a higher value of the horizontal pullout capacity P_H^* (**Fig. 8a**), and the maximum mobilized tension in the reinforcement T_{max}^* . Thus, the present analysis endorses the current practice of providing a well-compacted granular material as backfill (higher q_{ult}) for the construction of reinforced soil structures to mobilize a greater pullout resistance. Again, for a weaker subgrade (higher β), the end displacement W_L becomes very high (**Fig. 8b**) and may exceed the allowable limit. Thus, for all practical applications, the allowable end-displacement should also be a guiding factor in determining the design pullout capacity.

*6.3 Effect of Subgrade shear stiffness factor G**

Figures 9(a-b) show the effect of subgrade shear stiffness factor G^* on the normalized horizontal component of the oblique pullout force P_H^* and the end-displacement W_L. As G^* increases from 0 to 1000, all the above responses decrease from a maximum value at G^*= 0.

Figure 9(a) shows that as the subgrade shear stiffness factor G^*increases, the horizontal component of the oblique pullout force P_H^* decreases and, beyond a particular value of G^*, the value is almost unity (i.e. P_H^* equals the axial pullout capacity). The value of G^*, at which P_H^* becomes a unity, increases with the increase in ξ , μ, ϕ_r and α. A similar trend is also found for the end displacement (**Fig. 9b**) when G^* is varied.

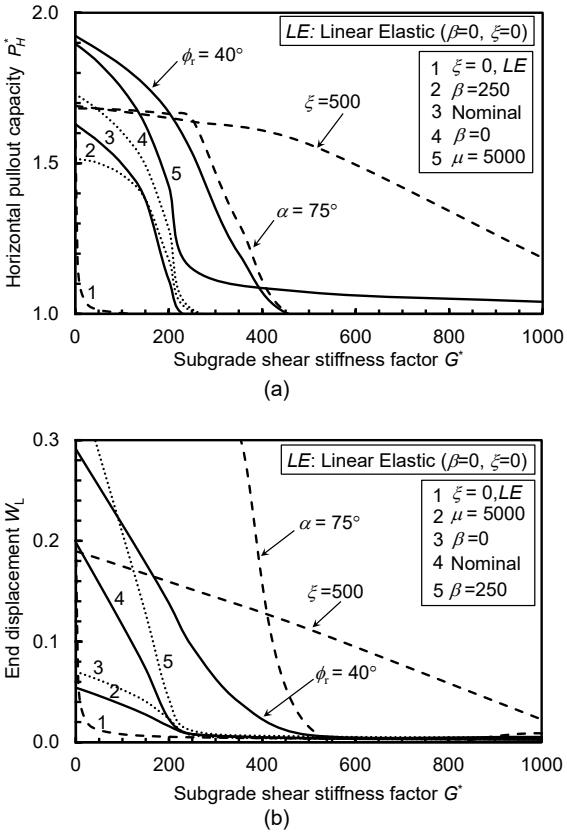

Fig. 9. Variation of (a) horizontal pullout capacity factor P_H^* ; and (b) end-displacement W_L with the subgrade shear stiffness factor G^* (Nominal case: μ=1000, ξ=100, β=100, ϕ_r=30°, α=60°).

For a particular value of the end-force P, as the subgrade shear stiffness G^* increases, a higher proportion of the load is distributed over the inner part of the subgrade by the shear interaction of the neighbouring soil elements. Thus, the generation of the normal stresses and the interface shear stresses decrease, resulting in a reduced value of the mobilized tension in the reinforcement. A lower reinforcement tension results in a lower value of the pullout capacity (**Fig. 9a**) and the end-displacement (**Fig 9b**).

6.4 Effect of Subgrade normal stiffness factor μ

Figure 10(a) shows that, as the subgrade normal stiffness factor μ increases, the horizontal component of the oblique pullout force P_H^* also increases. However, beyond a particular value of μ, the improvement is almost negligible due to the full mobilization of the interface shear stresses. The value of μ, at which P_H^* becomes virtually constant, increases with the increase in β (a weaker subgrade or decrease in the bearing resistance q_{ult}). Because, for a weaker subgrade (higher β), the displacements become more uniform throughout the length of the reinforcement thus, mobilizes lesser normal and the soil-reinforcement interface shear stresses. However, as μ increases, the reinforcement exhibits a more localized behaviour, giving rise to higher values of the interface shear stresses, which ultimately leads to a higher value of P_H^* . However, the end displacement W_L decreases (**Fig. 10b**) for higher values of μ as the subgrade becomes more incompressible in this case.

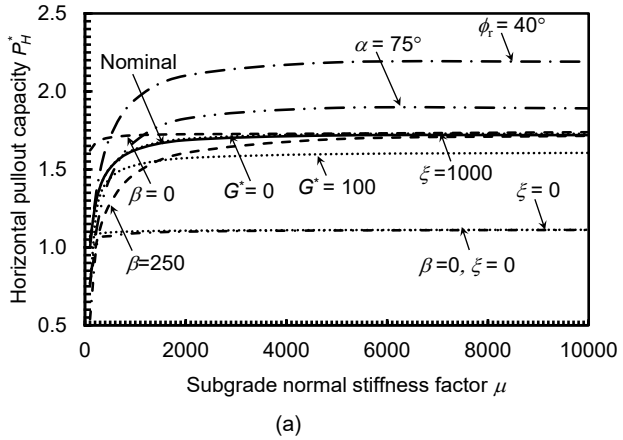

(a)

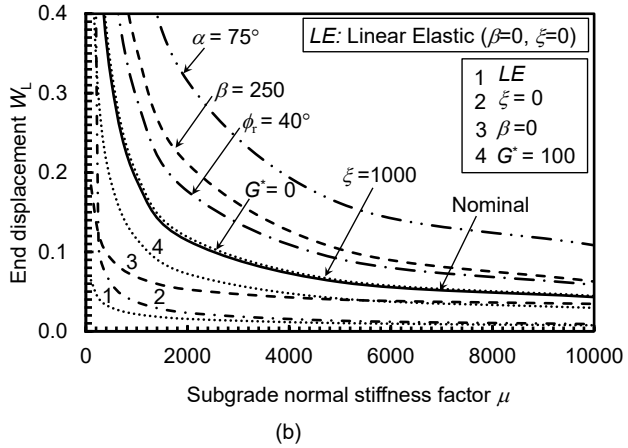

(b)

Fig. 10. Variation of (a) horizontal pullout capacity factor P_H^* ; and (b) end-displacement W_L with the subgrade normal stiffness factor μ (Nominal case: G^*=10, ξ=100, β=100, ϕ_r=30°, α=60°).

6.5 Effect of obliquity α of the pullout force

Figure 11 shows the effect of the obliquity α on the horizontal component of the pullout force P_H^* . As the obliquity α of the pullout force increases, P_H^* also increases. However, for α >60, the rate of increase in P_H^* reduces and even the trend is reversed as the value of P_H^* decreases for few cases, especially for weaker subgrade (or higher β). The reinforcement in these cases bends heavily, causing a reduction in the mobilized horizontal component of the soil-reinforcement interface shear stresses, which ultimately contributes to the lower value of P_H^* .

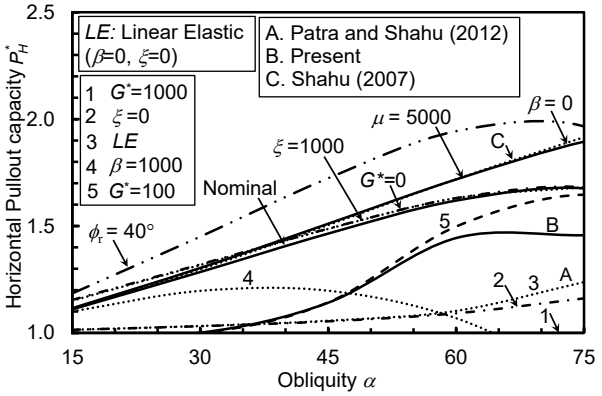

Fig. 11. Variation of horizontal pullout capacity factor P_H^* with the obliquity α (Nominal case: G^*=10, μ=1000, ξ=100, β=100 and ϕ_r=30°).

For a stiffer subgrade (higher G^* and lower ξ, i.e., G^* >100 and ξ < 100), P_H^* remains equal to the axial pullout force till a particular value of the obliquity α (refer curve 5, **Fig. 11**) is reached, beyond which, however, a sharp increase in the horizontal component of the pullout force P_H^* is observed. A stiffer subgrade also helps to reduce the bending of the reinforcement and distributes the displacement more uniformly over the length of the reinforcement. Since the displacement is distributed uniformly, the mobilized tension T^* increases linearly along the length of the reinforcement as in the case of the axial pullout. Consequently, the horizontal capacity of the pullout force P_H^* equals to the axial pullout capacity.

A comparison of results between the present analysis and that of Patra and Shahu (2012) are shown in **Figs. 9-11**. The results suggest that Patra and Shahu (2012) gives a highly conservative value of the end displacement, the reinforcement tension and the pullout capacity (curve A, **Fig. 11**) which are as low as 0.6 times the estimated value of the present analysis (curve B, **Fig. 11**). This may be due to the simplified linear elastic (ξ =0, β =0) assumption of the subgrade as proposed by Patra and Shahu (2012).

7. Conclusıons

A modified nonlinear analysis is presented to investigate the pullout response of geosynthetic reinforced soil (GRS) walls. The analysis considers a hyperbolic stress-strain relation for the backfill, the kinematics of the failure and the deformation compatibility between the soil and the reinforcement. The deformation compatibility is incorporated by introducing an updated discretization technique, and the true projected length of the reinforcement after deformation is evaluated by a simple computational scheme. The application of the present analysis is also shown with the example of a case study. The following conclusions are drawn:

• The present analysis is validated against a full-scale instrumented reinforced soil wall (Bathurst et al., 2009). The reinforcement load at each level was back-predicted using the present analysis and considering the effect of compaction. The results are also compared with the measured data (Bathurst et al., 2009) and AASHTO Simplified Method (AASHTO 2002). The comparison shows that the present analysis can be easily integrated with the existing method of analysis (AASHTO 2002) and gives a better estimation of the reinforcement tension at the pullout as compared to the AASHTO Simplified Method, and Patra and Shahu (2012). Note that Patra and Shahu (2012) underestimate the reinforcement tension in the top few reinforcements which are critical to the pullout failure.

• The present analysis shows that the reinforcement may undergo a significant deformation particularly, in the vicinity of the failure surface. However, Patra and Shahu (2012) estimated a highly conservative value of the end displacement, the reinforcement tension and the pullout capacity which may result from the simplified assumption of a linear elastic subgrade.

• For a given value of shear modulus G, a higher value of nonlinear subgrade response factor in shear ξ (= G/τ_{ult}) indicates a lower value of the ultimate failure shear stress τ_{ult} and a highly non-linear subgrade response in shear. As ξ increases (shear stiffness decreases), the horizontal component of the pullout force increases. For higher values of ξ (lower τ_{ult}), the shear layer ceases to distribute the normal stresses over a larger area thus the stresses at the soil-reinforcement interface becomes highly localized. Consequently, the interface shear stresses and the horizontal component of the pullout force increases. However, after a particular value of ξ, no significant improvement of P_H^* is observed as shear stresses between the neighbouring soil elements are fully mobilized.

• For the subgrade soil having a lower shear stiffness (lower G^* and ξ), the direction θ_L of the reinforcement tension sharply increases at the pullout end and becomes almost equal to the obliquity α of the pullout force (i.e. end angle $\theta_L \approx \alpha$). However, a stiffer subgrade (higher G^* and lower ξ) gives rise to a lower values of the end angle θ_L, as compared to the obliquity α of the pullout force.

• For a weaker subgrade (higher β) having lower normal and shear stiffness (lower μ and G^*, and higher ξ), the end displacement W_L becomes very high and may exceed the allowable limit. Thus, for all practical applications, the allowable end-displacement should be the guiding factor in determining the design pullout capacity for a weaker subgrade.

• For stiffer subgrade (higher G^* and lower ξ), P_H^* remains equal to the axial pullout force up to a particular value of the obliquity α of the pullout force. However, if the obliquity α exceeds this particular value, a sharp increase in the horizontal component of the pullout force is observed.

• The parametric study was conducted to quantify the effect of the stiffness (higher G^* and lower ξ) and the strength (lower values of β or higher q_{ult}) properties of the subgrade on the pullout responses. It is found that for all practical applications, both the strength, as well as the stiffness of the subgrade, should be considered to determine the design pullout capacity.

• The ranges of parameters used in the analysis corresponding to sand in the loose to dense state. The present approach is also applicable for other soil types. In that case, the soil-reinforcement adhesion should be added to the frictional component in the soil-reinforcement interface response (refer equation 2), and suitable elastic parameters E and ν should be adopted corresponding to the other soil type.

References

AASHTO 2002. Standard Specifications for Highway Bridges (Seventeenth Edition). Washington DC, USA: American Association of State Highway and Transportation Officials.

Ahmad, S.M., and Choudhury, D. 2012. Seismic internal stability analysis of waterfront reinforced-soil wall using pseudo-static approach. Ocean Engineering, Elsevier, **52**: 83-90.

Allen, T.M., and Bathurst, R.J. 2013. Design and Performance of 6.3-m-High, Block-Faced Geogrid Wall Designed Using K-Stiffness Method. Journal of Geotechnical and Geoenvironmental Engineering, **140** (2): 04013016.

Bathurst, R., Nernheim, A., Walters, D., Allen, T., Burgess, P., and Saunders, D. 2009. Influence of

reinforcement stiffness and compaction on the performance of four geosynthetic-reinforced soil walls. Geosynthetics International, **16** (1): 43-59.

Bergado, D.T., Teerawattanasuk, C. and Long, P.V. 2000. Localized mobilization of reinforcement force and its direction in the vicinity of failure surface. Geotextiles and Geomembranes, **18**: 311-331.

Bobet, A., Lee, H.S. and Santagata, M.C. 2007. Drained and undrained pullout capacity of a stiff inclusion in a saturated poroelastic matrix. International Journal for Numerical and Analytical Methods in Geomechanics, **31**: 715-734.

Damians, I.P., Bathurst, R.J., Adroguer, E.G., Josa, A. and Lloret, A. 2016. Environmental assessment of earth retaining wall structures. Environmental Geotechnics, Thomas Telford Ltd. http://dx.doi.org/10.1680/jenge.15.00040.

Desai, C.S., and El-Hoseiny, K.E. 2005. Prediction of field behavior of reinforced soil wall using advanced constitutive model. Journal of geotechnical and geoenvironmental engineering, American Society of Civil Engineers, **131** (6): 729-739.

Deb, K., Chandra, S. and Basudhar, P. 2007. Nonlinear analysis of multilayer extensible geosynthetic-reinforced granular bed on soft soil. Geotechnical and Geological Engineering, **25** (1): 11-23.

Elias, V., Christopher, B.R., and Berg, R.R. 2001. Mechanically stabilized earth walls and reinforced soil slopes - design and construction guidelines (Report FHWA-NHI-00-043). Washington, D.C: Federal Highway Administration (FHWA).

Gao, Y., Yang, S., Wu, Y., Li, D. and Zhang, F. 2014. Evaluation of oblique pullout resistance of reinforcements in soil wall subjected to seismic loads. Geotextiles and Geomembranes, **42** (5): 515-524.

Ghosh, C. and Madhav, M. 1994. Settlement response of a reinforced shallow earth bed. Geotextiles and Geomembranes, 13 (10): 643-656.

Gurung, N., Iwao, Y., and Madhav, M.R. 1999. Pullout test model for extensible reinforcement. International Journal for Numerical and Analytical Methods in Geomechanics, **23** (12): 1337-1348.

Huang, B., Bathurst, R.J., and Hatami, K. 2009. Numerical study of reinforced soil segmental walls using three different constitutive soil models. Journal of Geotechnical and Geoenvironmental engineering, 135 (10): 1486-1498.

Juran, I., and Christopher, B. 1989. Laboratory model study on geosynthetic reinforced soil retaining walls. Journal of Geotechnical Engineering, **115** (7): 905-926.

Kargar, M., and Hosseini, S. M.M.M. 2016. Influence of reinforcement stiffness and strength on load-settlement response of geocell-reinforced sand bases. European Journal of Environmental and Civil Engineering, Taylor and Francis, 1–18. http://dx.doi.org/10.1080/19648189.2016.1214181

Lee, K.L., Adams, B.D., and Vagneron, J.M.J. 1973. Reinforced earth retaining walls. Journal of Soil Mechanics and Foundation Division, **99**: 745-764.

Liu, H. 2016. Required reinforcement stiffness for vertical geosynthetic-reinforced-soil walls at strength limit state. Géotechnique, Thomas Telford Ltd, **66** (5): 424-434.

MacLaughlin, M., Sitar, N., Doolin, D., and Abbot, T. 2001. Investigation of slope-stability kinematics using discontinuous deformation analysis. International Journal of Rock Mechanics and Mining Sciences, **38**: 753-762.

Madhav, M, and Poorooshasb, H. 1989. Modified Pasternak model for reinforced soil. Mathematical and Computer Modelling, **12** (12): 1505-1509.

Madhav, M.R., and Umashankar, B. 2003a. Analysis of inextensible sheet reinforcement subject to transverse displacement/force: Linear subgrade response. Geotextiles and Geomembranes, **21** (2): 69-84.

Madhav, M., and Umashankar, B. 2003b. Analysis of inextensible sheet reinforcement subject to downward displacement/force: non-linear subgrade response. Geosynthetics International, **10** (3): 95-102.

Madhav, M.R., and Poorooshasb, H.B. 1988. A new model for geosynthetic reinforced soil. Computers and Geotechnics, **6** (4): 277-290.

National Concrete Masonry Association (NCMA) 1996. Design Manual for Segmental Retaining Walls (Second Ed.). Herndon, VA, USA: NCMA.

Patra, S., and Shahu, J.T. 2012. Pasternak model for oblique pullout of inextensible reinforcement. Journal of Geotechnical and Geoenvironmental Engineering, **138** (12): 1503-1513.

Patra, S., and Shahu, J.T. 2014. A new analysis of reinforced soil wall resting on soft ground. 9th International Symposium on Lowland Technology, September 29-October 1, 2014 in Saga, Japan, 348-352.

Patra, S., and Shahu, J.T. 2015a. Analysis of reinforced soil wall considering oblique pullout of reinforcement resting on two-parameter Pasternak subgrade. Geotechnical Special Publication, In M. Iskander, M. T. Suleiman, J. B. Anderson, D. F. Laefer (Editors), proceedings of the International Foundations Congress and Equipment Expo (IFCEE 2015), March 17-21, 2015, San Antonio, Texas: 1464-1472.

Patra, S., and Shahu, J.T. 2015b. Behaviour of extensible reinforcement resting on non-linear

Pasternak subgrade subjected to oblique pull. Géotechnique, **65** (9): 770–779.

Poorooshasb, H., Pietruszczak, S., and Ashtakala, B. 1985. An extension of the Pasternak foundation concept. Soils and foundations, **25** (3): 31-40.

Ouria, A., Toufigh, V., Desai, C., Toufigh, V., and Saadatmanesh, H. 2016. Finite element analysis of a CFRP reinforced retaining wall. Geomechanics and Engineering, **10** (6): 757-774.

Rowe, R.K., and Ho, S.K. 1993. Keynote lecture: A review of the behaviour of reinforced soil walls. Proc. In H. Ochiai, S. Hayashi, and J. Otani (Editors), Int. Symp. on Earth Reinforcement Practice, Balkema, Rotterdam, Vol. 2: 801-830.

Shahu, J.T. 2007. Pullout response of inextensible sheet reinforcement subject to oblique end-force. Journal of Geotechnical and Geoenvironmental Engineering, **133** (11): 1440-1448.

Shahu, J.T. 2008. Inextensible reinforcement on non-linear elasto-plastic subgrade under oblique pull. International journal for numerical and analytical methods in geomechanics, **32**: 2067-2081.

Shahu, J.T. and Hayashi, S. 2009. Analysis of extensible reinforcement subject to oblique pull. Journal of geotechnical and geoenvironmental engineering, **135** (5): 623–634.

Shewbridge, S.E., and Sitar, N. 1989. Deformation characteristics of reinforced sand in direct shear. Journal of Geotechnical Engineering, **115**: 1134-1147.

Shukla, S.K., and Chandra, S. 1994. A generalized mechanical model for geosynthetic-reinforced foundation soil. Geotextiles and Geomembranes, **13**: 813-825.

Sitar, N., MacLaughlin, M.M., and Doolin, D.M. 2005. Influence of kinematics on landslide mobility and failure mode. Journal of geotechnical and geoenvironmental engineering, **131**: 716-728.

Sowmiya, L.S., Shahu, J.T., and Gupta K.K. 2015. Performance of geosynthetic reinforcement on the ballasted railway track. Lowland Technology International, **17** (2): 83-92.

Tanahashi, H. 2007. Pasternak model formulation of elastic displacements in the case of a rigid circular foundation. Journal of Asian Architecture and Building Engineering, **6**: 167-173.

Won, M.S., Lee, O.H., Kim, Y.S., and Choi, S.K. 2016. A 12-year long-term study on the external deformation behavior of Geosynthetic Reinforced Soil (GRS) walls. Geomechanics and Engineering, **10** (5): 565-575.

Yu, Y., Bathurst, R.J., and Allen, T.M. 2016. Numerical Modeling of the SR-18 Geogrid Reinforced Modular Block Retaining Walls. Journal of Geotechnical and Geoenvironmental Engineering, **142** (5): 04016003-1-13.

Symbols and abbreviations

α	Obliquity of the end-force
β	Nonlinear subgrade response factor in vertical compression= $k_s L/q_{ult}$
D	Overburden depth (m)
Δx	Length of reinforcement element along x-axis (m)
E_s	Modulus of elasticity of soil (kN/m^2)
ϕ	Angle of shearing resistance of soil
ϕ_r	Angle of interface shearing resistance between soil and reinforcement
G	Shear modulus (kN/m^2)
γ	Unit weight of the soil (kN/m^3)
G^*	Subgrade shear stiffness factor= $GH/\gamma DL$
H	Shear layer thickness (m)
J	Reinforcement stiffness (kN/m)
J^*	Reinforcement stiffness factor
ξ	Nonlinear subgrade response factor in shear = G/τ_{ult}
k_s	Modulus of subgrade reaction or spring constant (kN/m^3)
K_a	Active earth pressure coefficient
L	Reinforcement length (m)
L_H	Horizontal projected length (m)
μ	Subgrade normal stiffness factor = $k_s L/\gamma D$
n	Total number of elements
ν	Poisson's ratio
p, q	Vertical stresses at the top and the bottom surfaces of reinforcement (kN/m^2)
P	Oblique end-force (kN/m)
P^*	Normalized oblique pullout force = P/T_{HP}
P_H^*	Normalized horizontal component of oblique pullout force
q_{ult}	Ultimate normal/compressive strength of the subgrade (kN/m^2)
τ_t, τ_b	Friction stresses or soil-reinforcement interface shear resistance on the top and bottom surface of the reinforcement (kN/m^2)
τ_{ult}	Ultimate shear strength of the subgrade (kN/m^2)
T, $T+\Delta T$	Tension in the reinforcement at distance x and $x+\Delta x$ respectively (kN/m)
T_{HP}	Axial pullout capacity = $2\gamma DL\tan\phi_r$ (kN/m)
$T_{\max}^*$	Normalized maximum tension in reinforcement
θ, $\theta+\Delta\theta$	Slope of reinforcement with horizontal at distance x and $x+\Delta x$
T_{HP}	Axial pullout capacity of the reinforcement
T^*	Normalized tension = T/T_{HP}

w	Vertical displacement of the reinforcement (m)
W	Normalized displacement = w/w_L
x, z	Horizontal and vertical axes
X	Normalized distance = x/L

Subscripts

c	Center
H	Horizontal component
i	Node or element or iteration
L	Value at $X = 1$
Max	Maximum
0	Value at $X = 0$
X	Horizontal direction